Computation of Vortex-Dominated Flow for a Delta Wing Undergoing Pitching Oscillation

Osama A. Kandil* and H. Andrew Chuang†
Old Dominion University, Norfolk, Virginia

The conservative, unsteady Euler equations for the flow relative to a moving frame of reference are used to solve for the three-dimensional steady and unsteady flows around a sharp-edged delta wing. The resulting equations are solved by using an implicit, approximately factored, finite-volume scheme. Implicit second-order and explicit second- and fourth-order dissipations are added to the scheme. The boundary conditions are explicitly satisfied. The grid is generated by locally using a modified Joukowski transformation in crossflow planes at the grid-chord stations. The computational applications cover a steady flow around a delta wing, whose results serve as the initial conditions for the unsteady flow around a pitching delta wing at a large mean angle of attack. The steady results are compared with the experimental data, and the unsteady results are compared with results of a flux-difference splitting scheme.

Introduction

UNSTEADY flows around delta wings are characterized by the existence of unsteady large- and small-scale vortices (primary, secondary, and possible tertiary vortices), moving shock waves with time-dependent strengths, time-dependent vortex-core formation and breakdown (bubble and spiral types of vortex breakdown), and interaction of shock waves with the vortical-region and the surface-boundary-layer flows. These highly unsteady aerodynamic loads may interact with the wing structural response causing aeroelastic instabilities, which may restrict the aircraft flight envelope. In Ref. 1, the status of computational unsteady aerodynamics for aeroelastic analysis has been discussed, and recommendations for future code development for separated and vortex-dominated flows are presented.

The literature on the computational solution and experimental data of the unsteady, vortex-dominated flows, particularly in the transonic regime, is unfortunately very limited. This is attributed to the complexity of the flow and its dependence on numerous parameters and the substantial computational cost involved for the flow resolution and the time-accurate computations.

Most of the existing unsteady computational schemes for airfoil and wing flow applications are based on the unsteady small disturbance (UTSD) theory,[2-4] unsteady full potential (UFP) equation,[5-7] UTSD theory with vorticity and nonisentropic flow corrections,[8] and UFP equation with nonisentropic flow corrections.[9] These schemes are restricted to attached flows only, and hence they cannot be used to capture vortex-dominated flows. For mildly separated flows, integral and finite-difference boundary-layer schemes have been coupled with potential flow schemes.[10,11] However, such schemes cannot be used for massive separation.

On the other hand, the unsteady Euler equations adequately model shock waves and their motion, entropy increase across shocks, and entropy gradient and vorticity production and convection behind shocks, as can be seen from Crocco's theorem and the inviscid vorticity transport equation. Moreover, the computational solution of Euler equations adequately models separated flows from sharp edges.[12-14] For smooth-surface separation, round-edge separation, shock-induced separation, viscous diffusion and dissipation, vortex breakdown, flow transition, and turbulence, viscous terms must be added to Euler equations to recover the full Navier-Stokes equations or an approximate form of these equations. Although the process of adding the viscous terms to the unsteady Euler solvers is simple and straightforward, the computational cost for high-Reynolds-number unsteady flows is substantial and might be prohibitive due to the need for using fine grids to adequately resolve the viscous effects.

Euler/Navier-Stokes zonal approaches[15,16] have been demonstrated to maintain the accuracy of the Navier-Stokes solutions and, in the meantime, to alleviate to a good extent the computational cost of the Navier-Stokes equations. These approaches along with fine-grid embedding in the vortical regions should be developed further for unsteady flows.

Recently, successful time-accurate solutions of the unsteady Euler and Navier-Stokes equations have been presented for airfoils.[14,17-20] The only existing unsteady Euler solutions for vortex-dominated flows are those for the rolling oscillation of a sharp-edge delta wing in a locally conical supersonic flow around a mean angle of attack and a zero angle of attack, which were presented by the authors in Refs. 13 and 14. The authors derived the unsteady Euler equations for the flow relative to a moving frame of reference, and the equations have been solved by using an explicit, multistage Runge-Kutta time-stepping, finite-volume scheme. By casting the equations in a moving frame of reference, we eliminated the computation of the grid motion. Moreover, since the equations are expressed in terms of the flow vector field relative to the moving frame, the equations still preserve the conservation form. Periodic solutions were achieved in the third cycle of rolling oscillation. Details of the surface pressure, crossflow velocity, and crossflow Mach contours were presented showing the primary-vortex and shock-wave formation, interaction, and dissappearance.

In the present paper, the three-dimensional, unsteady Euler equations in a moving frame of reference are solved by using an implicit approximately factored, finite-volume scheme. The resulting code has been validated through the solution of unsteady flows around airfoils undergoing pitching oscillation[17] and comparison of the computed results with the experimental data of Ref. 21. The present three-dimensional steady results are compared with the experimental data of

Received Nov. 28, 1988; revision received Oct. 3, 1989.

*Professor, Department of Mechanical Engineering and Mechanics. Associate Fellow AIAA.

†Visiting Assistant Professor, Department of Mechanical Engineering and Mechanics. Member AIAA.

Ref. 22 for two levels of explicit dissipation. With the steady results serving as initial conditions for the unsteady flow, the flow around the same delta wing undergoing pitching oscillation about the quarter-chord axis is solved in this paper. The results of the pitching delta wing are compared with those obtained using the three-dimensional, flux-difference splitting scheme of Ref. 20.

Formulation

Starting with the conservative form of the unsteady Euler equations for the flow relative to a space-fixed frame of reference, and using the following relations for the substantial and local derivatives of a scalar a and a vector $\bar{A}$,

$$\frac{Da}{Dt} = \frac{D'a}{Dt'} \tag{1a}$$

$$\frac{\partial a}{\partial t} = \frac{\partial' a}{\partial t'} - \bar{V}_t \cdot \nabla a \tag{1b}$$

$$\frac{D\bar{A}}{Dt} = \frac{D'\bar{A}}{Dt'} + \bar{\omega} \times \bar{A} \tag{1c}$$

$$\frac{\partial \bar{A}}{\partial t} = \frac{\partial' \bar{A}}{\partial t'} - \bar{V}_t \cdot \nabla \bar{A} + \bar{\omega} \times \bar{A} \tag{1d}$$

we obtain the conservative unsteady Euler equations for the flow relative to a moving frame of reference. In terms of the Cartesian coordinates x', y', and z' of the moving frame of reference, the resulting Euler equations are

$$\frac{\partial' \bar{q}_r}{\partial t'} + \frac{\partial' \bar{E}_r}{\partial x'} + \frac{\partial' \bar{F}_r}{\partial y'} + \frac{\partial' \bar{G}_r}{\partial z'} = \bar{S} \tag{2}$$

where

$$\bar{q}_r = [\rho, \rho u_r, \rho v_r, \rho w_r, \rho e_r]^t \tag{3}$$

$$\bar{E}_r = [\rho u_r, \rho u_r^2 + p, \rho u_r v_r, \rho u_r w_r, \rho u_r h_r]^t \tag{4}$$

$$\bar{F}_r = [\rho v_r, \rho u_r v_r, \rho v_r^2 + p, \rho v_r w_r, \rho v_r h_r]^t \tag{5}$$

$$\bar{G}_r = [\rho w_r, \rho u_r w_r, \rho v_r w_r, \rho w_r^2 + p, \rho w_r h_r]^t \tag{6}$$

$$\bar{S} = [0, -\rho a_{tx'}, -\rho a_{ty'}, -\rho a_{tz'}, -\rho[\bar{V}_r \cdot \bar{a}_0 + (\bar{\omega} \times \bar{r}) \cdot \bar{a}_0 + \bar{V}_0 \cdot (\bar{a}_t - \bar{\omega} \times \bar{V}_r) + \bar{V}_r \cdot (\dot{\bar{\omega}} \times \bar{r}) + (\bar{\omega} \times \bar{r}) \cdot (\dot{\bar{\omega}} \times \bar{r})]]^t \tag{7}$$

$$e_r = e - \bar{V} \cdot \bar{V}_t = \frac{p}{\rho(\gamma - 1)} + \frac{V_r^2}{2} - \frac{V_t^2}{2} \tag{8}$$

$$h_r = h - \bar{V} \cdot \bar{V}_t = \frac{\gamma p}{\rho(\gamma - 1)} + \frac{V_r^2}{2} - \frac{V_t^2}{2} \tag{9}$$

$$\bar{V}_t = \bar{V} - \bar{V}_r = \bar{V}_0 + \bar{\omega} \times \bar{r} \tag{10}$$

$$\bar{a}_t = \bar{a} - \bar{a}_r = \frac{D\bar{V}}{Dt} - \frac{D'\bar{V}_r}{Dt'} = \bar{a}_0 + \dot{\bar{\omega}} \times \bar{r} + 2\bar{\omega} \times \bar{V}_r + \bar{\omega} \times (\bar{\omega} \times \bar{r}) \tag{11}$$

$$\bar{\omega} = \omega_{x'}\hat{i} + \omega_{y'}\hat{j} + \omega_{z'}\hat{k} = (-\dot{\alpha} \sin\beta + \dot{\theta})\hat{i} + (\dot{\alpha} \cos\beta \sin\theta + \dot{\beta} \cos\theta)\hat{j} + (\dot{\alpha} \cos\beta \cos\theta - \dot{\beta} \sin\theta)\hat{k} \tag{12}$$

In Eqs. (1–12), $\bar{q}_r$ is the flow vector field of relative motion; $\bar{E}_r$, $\bar{F}_r$, and $\bar{G}_r$ the inviscid fluxes of the relative motion, $\bar{S}$ a source term due to the motion of the reference frame, ρ the density, p the pressure, e and h the total energy and total enthalpy per unit mass, $\bar{V}$ and $\bar{a}$ the absolute velocity and absolute acceleration of the flow, $\bar{V}_r$ and $\bar{a}_r$ the flow relative velocity and relative acceleration, $\bar{V}_t$ and $\bar{a}_t$ the transformation velocity and transformation acceleration, $\bar{V}_0$ and $\bar{a}_0$ the translation velocity and translation acceleration of the moving frame, $\bar{\omega}$ and $\dot{\bar{\omega}}$ the angular velocity and angular acceleration of the moving frame, $\bar{r}$ the position vector of a fluid particle with respect to the moving frame, and γ is the ratio of specific heats. The pitch, yaw, and roll angles are referred to by using the Eulerian angles α, β, and θ, respectively. The $(')$ refers to the derivatives, time, or coordinates with respect to the moving frame of reference. Equation (2) shows that the present formulation is in a conservation form. However, the conservation form is not a strong one due to the existence of the source term on the right side. But on the other hand, the Jacobian corresponding to this term is not spatially differenced [see Eqs. (21) and (22)], and hence the truncation error of this term is mainly due to temporal differencing.

Introducing the curvilinear coordinates ξ', η', and ζ' in the moving frame of reference, which are given by

$$\xi' = \xi'(x', y', z'), \qquad \eta' = \eta'(x', y', z'), \qquad \zeta' = \zeta'(x', y', z') \tag{13}$$

Eqs. (2–7) are transformed to

$$\frac{\partial' \hat{Q}_r}{\partial t'} + \frac{\partial' \hat{E}_r}{\partial \xi'} + \frac{\partial' \hat{F}_r}{\partial \eta'} + \frac{\partial' \hat{G}_r}{\partial \zeta'} = \hat{S} \tag{14}$$

$$\hat{Q}_r = J^{-1}[\rho, \rho u_r, \rho v_r, \rho w_r, \rho e_r]^t \tag{15}$$

$$\hat{E}_r = J^{-1}[\rho U_r, \rho u_r U_r + \xi'_{x'} p, \rho v_r U_r + \xi'_{y'} p, \rho w_r U_r + \xi'_{z'} p, \rho U_r h_r]^t \tag{16}$$

$$\hat{F}_r = J^{-1}[\rho V_r, \rho u_r V_r + \eta'_{x'} p, \rho v_r V_r + \eta'_{y'} p, \rho w_r V_r + \eta'_{z'} p, \rho V_r h_r]^t \tag{17}$$

$$\hat{G}_r = J^{-1}[\rho W_r, \rho u_r W_r + \zeta'_{x'} p, \rho v_r W_r + \zeta'_{y'} p, \rho w_r W_r + \zeta'_{z'} p, \rho W_r h_r]^t \tag{18}$$

$$\hat{S} = J^{-1}\bar{S} \tag{19}$$

In Eqs. (15–19), J^{-1} is the Jacobian of transformation, and U_r, V_r, and W_r are the contravariant velocity components.

Computational Scheme

Equation (14) is integrated over ξ', η', and ζ', and the divergence theorem is applied to the resulting equation. By using the implicit approximate factorization scheme, we obtain the following difference equation for a typical cell (i,j,k)

$$\left[\frac{I}{J\,\Delta t'} + \delta_{\xi'} A_r^n - \frac{H_r^n}{J} - D_{m\xi'}\right]\left[\frac{I}{J\,\Delta t'} + \delta_{\eta'} B_r^n - D_{m\eta'}\right] \times \left[\frac{I}{J\,\Delta t'} + \delta_{\zeta'} C_r^n - D_{m\zeta'}\right]\Delta q_r^n = -\frac{1}{(J\,\Delta t')^2}\bar{W}(\bar{q}_r^n) \tag{20}$$

where

$$\bar{W}(\bar{q}_r^n) = (\hat{E}^n_{r_{i+1/2,j,k}} - \hat{E}^n_{r_{i-1/2,j,k}}) + (\hat{F}^n_{r_{i,j+1/2,k}} - \hat{F}^n_{i_{i,j-1/2,k}}) + (\hat{G}^n_{r_{i,j,k+1/2}} - \hat{G}^n_{r_{i,j,k-1/2}}) - \hat{S}^n_{i,j,k} - D_{e\xi'}(\bar{q}_r^n) - D_{e\eta'}(\bar{q}_r^n) - D_{e\zeta'}(\bar{q}_r^n) \tag{21}$$

In Eqs. (20) and (21), A_r, B_r, C_r, and H_r are the Jacobian matrices $\partial\hat{E}_r/\partial\bar{q}_r$, $\partial\hat{F}_r/\partial\bar{q}_r$, $\partial\hat{G}_r/\partial\bar{q}_r$, and $\partial\bar{S}/\partial\bar{q}_r$, respectively; $\delta_{\xi'}$, $\delta_{\eta'}$, and $\delta_{\zeta'}$ the three-point, central-difference operators; $D_{m\xi'}$, $D_{m\eta'}$, and $D_{m\zeta'}$ the implicit dissipation operators; and $D_{e\xi'}$, $D_{e\eta'}$, and $D_{e\zeta'}$ the explicit dissipation operators. The expressions of the dissipation operators in the ξ' direction are given by

$$D_{m\xi'} = \varepsilon_m I \left(\frac{CFL}{J\,\Delta t'}\right)(\Delta\nabla)_{\xi'} \tag{22}$$

$$D_{e\xi'} = \nabla_{\xi'}\left(\frac{J^{-1}_{i+1,j,k}}{\Delta t^*_{i+1,j,k}} + \frac{J^{-1}_{i,j,k}}{\Delta t^*_{i,j,k}}\right)(\nu^{(2)}_{i,j,k}\Delta_{\xi'} - \nu^{(4)}_{i,j,k}\Delta_{\xi'}\nabla_{\xi'}\Delta_{\xi'}) \tag{23}$$

$$\nu^{(2)}_{i,j,k} = \varepsilon_2 \max(\lambda_{i+1,j,k}, \lambda_{i,j,k}) \tag{24}$$

$$\nu^{(4)}_{i,j,k} = \max(0, \varepsilon_4\,\Delta t^* - \nu^{(2)}_{i,j,k}) \tag{25}$$

$$\lambda_{i,j,k} = \frac{|P^n_{i+1,j,k} - 2P^n_{i,j,k} + P^n_{i-1,j,k}|}{|P^n_{i+1,j,k} + 2P^n_{i,j,k} + P^n_{i-1,j,k}|} \tag{26}$$

$$\Delta t^* = \frac{\Delta t'}{CFL} = \frac{1}{|U_r| + |V_r| + |W_r| + a(|\nabla\xi'| + |\nabla\eta'| + |\nabla\zeta'|)} \tag{27}$$

where U_r, V_r, and W_r are the contravariant components of the relative velocity. The implicit-damping coefficient is ε_m, and the explicit-damping coefficients are ε_2 and ε_4. The damping coefficients are having the same values in the ξ', η', and ζ' directions.

The solution of Eq. (20) is obtained through three successive sweeps in the η', ζ', and ξ', respectively. Once $\Delta\bar{q}^n_r$ is obtained, $\bar{q}^{n+1}_r$ is found from

$$\bar{q}^{n+1}_r = \bar{q}^n_r + \Delta\bar{q}^n_r \tag{28}$$

Boundary Conditions

The surface-boundary condition is enforced explicitly through the normal momentum equation

$$\frac{\partial p}{\partial n} = \rho\bar{V}_r \cdot (\bar{V}_r \cdot \nabla\hat{n}) - \rho\hat{n} \cdot \bar{a}_t \tag{29}$$

where $\hat{n}$ is the unit normal of the wing surface. Also, the far-field boundary conditions are enforced explicitly. In the present application, subsonic flow in the far field is considered and hence, the inflow-outflow boundary conditions are based on the Riemann invariants, R_∞ and R_i, for one-dimensional flow normal to the boundary, which are given by

$$R_\infty = \bar{V}_\infty \cdot \hat{n} - \frac{2}{\gamma - 1}(\gamma p_\infty/\rho_\infty)^{1/2} \tag{30}$$

$$R_i = \bar{V}_i \cdot \hat{n} + \frac{2}{\gamma - 1}(\gamma p_i/\rho_i)^{1/2} \tag{31}$$

where $\hat{n}$ is the unit normal of the outer boundary of the computational region, and the subscripts ∞ and i refer to the far-field conditions and the values extrapolated from the interior cells at the boundary, respectively. Thus, the inflow boundary conditions are given by

$$(\bar{V} \cdot \hat{n})_b = \tfrac{1}{2}(R_\infty + R_i) \tag{32a}$$

$$\left(\frac{p}{\rho}\right)_b = \frac{1}{\gamma}\left[\frac{\gamma - 1}{4}(R_i - R_\infty)\right]^2 \tag{32b}$$

$$(p/\rho^\gamma)_b = (P/\rho^\gamma)_\infty \tag{32c}$$

$$(\bar{V} \cdot \hat{t})_b = (\bar{V} \cdot \hat{t})_\infty \tag{32d}$$

where b refers to the boundary, and $\hat{t}$ is a unit-vector tangential to the boundary. For the outflow boundary conditions, the subscript ∞ in Eqs. (32c) and (32d) is replaced by the subscript i. Equations (32a) and (32b) give a complete definition of the flow at subsonic boundaries. Symmetric flow conditions are used at the plane of symmetry for the present application.

Computational Results

A sharp-edged delta wing of aspect ratio (AR) of one at a mean angle of attack α_m of 20.5 deg and a freestream Mach number M_∞ of 0.3 is considered for the computational application of the implicit, three-dimensional vectorized program. The body conformed grid consists of 80 × 38 × 48 cells in the ξ', η', and ζ' directions, respectively, and its size is one root chord ahead of the wing vertex, two root chords behind the trailing edge, and one root-chord radius in the crossflow planes. The size of the computational domain has been determined through numerical experiments, where the maximum absolute value of the difference of the pressure coefficient did

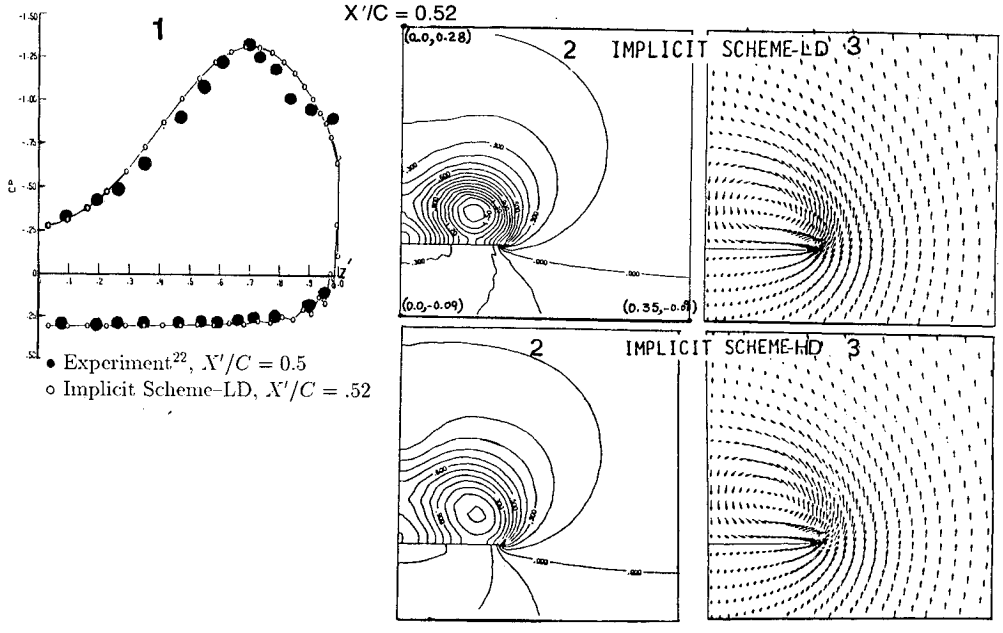

Fig. 1 Comparison of the surface-pressure, static-pressure contours, and crossflow velocity at chord station $X'/C = 0.52$.

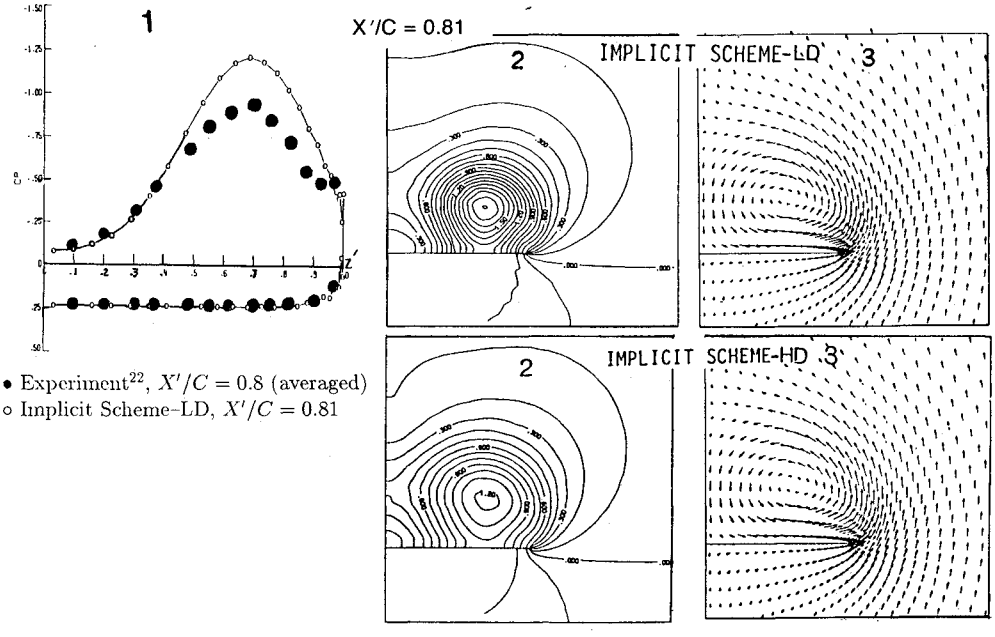

Fig. 2 Comparison of the surface-pressure, static-pressure contours, and crossflow velocity at chord station $X'/C = 0.81$.

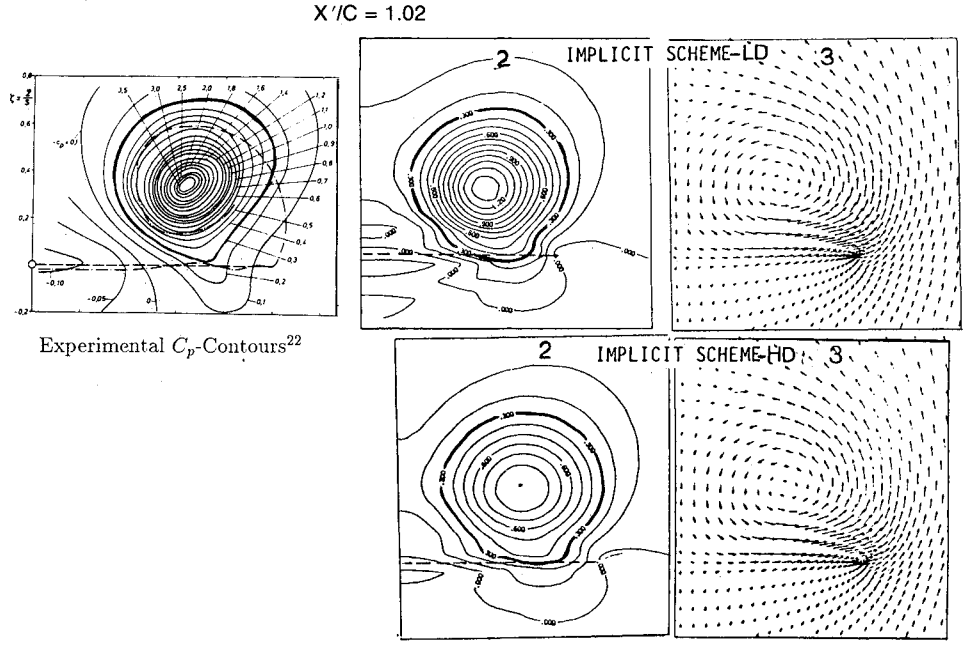

Fig. 3 Comparison of the static-pressure contours and crossflow velocity at chord station $X'/C = 1.02$ in the wake.

not exceed 0.5% from that of a computational domain, which has double the present computational size. The small computational domain is used because of the limited available computational resources. The outer boundary consists of a hemispherical surface with its center at the wing vertex and a cylindrical surface with its axis coinciding with the wing axis. The grid is generated in crossflow planes using a modified Joukowski transformation, which is locally applied at the grid-chord stations with exponential clustering at the wing surface.

Steady Flow

The implicit program is used to solve for the steady flow at a 20.5-deg angle of attack with two levels of numerical dissipation: a low dissipation (LD) with $\varepsilon_2 = 0.05$, $\varepsilon_4 = 0.0025$, and $\varepsilon_m = 0.25$ and a high dissipation (HD) with $\varepsilon_2 = 0.25$, $\varepsilon_4 = 0.0025$, and $\varepsilon_m = 0.25$. As a general principle, the dissipation level in a computational scheme must be as low as possible. But it must be enough to obtain a stable solution. Although we are dealing with a low subsonic flow, where shocks do not exist, second-order dissipation terms are required due to the large gradients in the vortical region. The purpose of this numerical experiment is to determine a LD level, which gives a stable solution also. Figures 1 and 2 show the solutions at two chord stations of 0.52 and 0.81 on the wing, respectively. The figures from left to right show the surface-pressure coefficient (see part 1 in Figs. 1 and 2), the static-pressure coefficient contours (see part 2 in Figs. 1 and 2), and the crossflow velocity directions (see part 3 in Figs. 1 and 2). Here, we compare the surface pressure of the implicit scheme with LD with that of the experimental data of Hummel.[22] Other comparisons are given by the authors in Ref. 24.

In Fig. 1, the computed surface pressure with LD is in excellent agreement with the experimental data. The com-

puted static pressure contours with LD show higher pressure levels than those computed contours with HD—particularly in the vortical core region. With LD, the highest pressure contour is 1.6, and with HD the highest pressure contour (at the same location) is 1.1. The crossflow velocities of both dissipation levels show almost identical shapes and directions. Comparison of the computed surface pressure with HD with that of the experimental data (given in Ref. 24) shows that the computed peak-suction pressure is underpredicted by 18%; although the remainder of the surface pressure is in good agreement with the experimental data.

In Fig. 2, the computed surface pressure with LD is higher than that of the experimental data—particularly under the primary vortex core. It should be noted here that the experimental data of Hummel shown in part 1 of Fig. 2 is the average of his data at $X'/C = 0.7$ and 0.9 in Ref. 22. The computed peak-suction pressure is about 25% higher than that of the experimental data. Comparison of the computed static pressure contours with LD shows higher pressure levels than those computed contours with HD—particularly in the vortical core region. With LD, the highest pressure contour is 1.7, and with HD, the highest pressure contour is 1.2. The crossflow velocities of both dissipation levels show almost identical shapes and directions.

Figures 3 and 4 show the experimental, static, pressure-coefficient contours of Hummel[22] in planes perpendicular to the wind direction (see part 1 of Figs. 3 and 4), the computed, static, pressure-coefficient contours in planes perpendicular to the wing surface (see part 2 of Figs. 3 and 4) and the crossflow velocity directions (see parts 3 and 4 of Fig. 4). The computational results along with the experimental data are shown for two crossflow planes in the wake: $X'/C = 1.02$ and $X'/C = 1.25$. In Fig. 3, the computed, static-pressure contours of the outer vortex-core region are in excellent agreement with the experimental contours. For the most inner static-pressure contours (levels higher than 0.3), the experimental data show a higher level than those of the computed results. On the other hand, the results of static-pressure contours of the implicit scheme with LD show higher pressure levels than those with the HD. Similar results are seen at $X'/C = 1.25$ (see Fig. 4). At this location, it is seen that the outer contour of the trailing-edge vortex core is captured using the LD, implicit scheme (contour level of 0.4). The crossflow velocities at $X'/C = 1.25$ also show that the trailing-edge vortex core has been captured.

The discrepancies between the experimental data and the computed results with an LD level are attributed to the grid coarseness in the vortical core and more important to neglecting the viscous effects in the vortex core as well as on the wing upper surface. The discrepancies between the computed results with LD and HD are obviously due to the low and high value of the explicit, second-order damping coefficient.

On the VPS-32 computer of the NASA Langley Research Center, the CPU time is 40 μs per grid point per time step and a typical steady-flow case takes 1050 pseudotime stepping to reach a residual error of 10^{-3}.

Unsteady Flow, Pitching Oscillation about the Quarter-Chord Axis

The steady results with an LD level, the best level for a stable solution, are used as the initial conditions for calculating the unsteady flow around the same wing which is undergoing a pitching oscillation about the quarter-chord axis. The angle of attack $\alpha(t)$ is given by

$$\alpha(t) = \alpha_m + \alpha_0 \sin 2\sqrt{\gamma} M_\infty kt \tag{33}$$

where α_0 is the amplitude, and k is the reduced frequency ($k = k^*C/2U_\infty$, $k^* \equiv$ dimensional frequency and $c \equiv$ wing-chord length). In this application $\alpha_m = 20.5$ deg, $\alpha_0 = 2$ deg, $M_\infty = 0.3$, and $k = 3$, which corresponds to a period of 2.95 per cycle. Each cycle of oscillation takes about 1475 time steps, and the solution covers 5000 time steps, which correspond to 3.39 cycles of oscillation.

Figure 5 shows α vs t motion at the top, which is followed by the surface pressure variation, static-pressure contours, and crossflow velocity in each row of figures. The numbers 1–15 on the α-t curve and on the other figures indicate the instants at which the computational results are shown. Here, we show the computations at the chord station $X'/C = 0.52$, and the computed surface pressures are shown every 200 time steps starting from the 2200 time step, which corresponds to point 1 on the α-t curve. The static-pressure contours and the crossflow velocity directions are given at the 3000, 4000, and 5000 time steps, which correspond to points 5, 10, and 15, respectively, on the α-t curve. Comparison of the surface pressure at points 7 and 14 on the α-t curve corresponding to

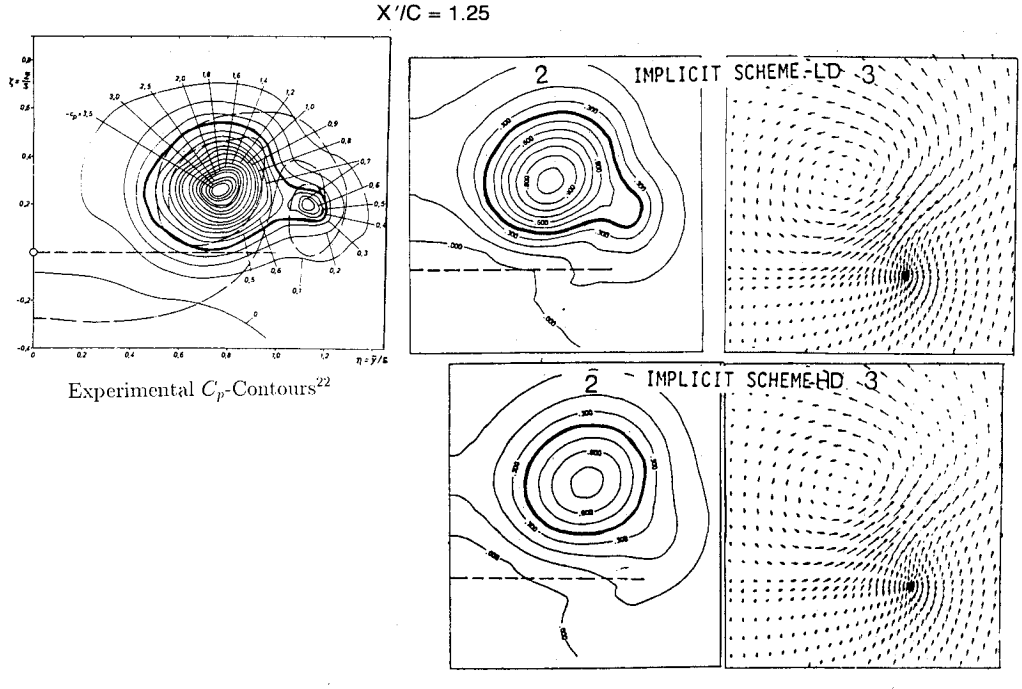

Fig. 4 Comparison of the static-pressure contours and crossflow velocity at chord station $X'/C = 1.25$ in the wake.

2.31 and 3.25 cycles, respectively, shows that periodic oscillation has already been reached.

Considering the time history of the surface pressures, which are indicated by the numbers 1–5, 6–10, and 11–15, the variation of the surface pressure and the motion of the primary vortex are predicted as the wing pitching motion is progressing. For example, the curves 1–5 show that as the angle of attack increases from instant 1 to instant 2, the peak suction pressure increases, and the primary vortex moves outboard in the spanwise direction. This is physically expected since the primary vortex strength increases. As the angle of attack increases from instant 2 to instant 3, the peak suction pressures reach a maximum value and then decrease, indicating that the peak suction pressure is leading the wing motion. As the angle of attack decreases from instant 3 to instant 5, the peak suction pressure decreases, and the primary vortex moves inboard in the spanwise direction.

On the surface pressure curves, we also show comparisons at selected instants with the computations of Rumsey.[25] Rumsey's computations are produced using a three-dimensional, implicit, flux-difference splitting program, which is known as "CFL3D." The results are computed by using our grid, which is used to compute our results. The results are in good agreement and, hence, the comparison adds confidence to the computational prediction. Experimental data for the unsteady, vortex-dominated wing flows are urgently needed for bench-mark comparisons. However, it is emphasized here that our present scheme and code have been validated earlier[17] for unsteady flows around pitching airfoils using available experimental data.[21]

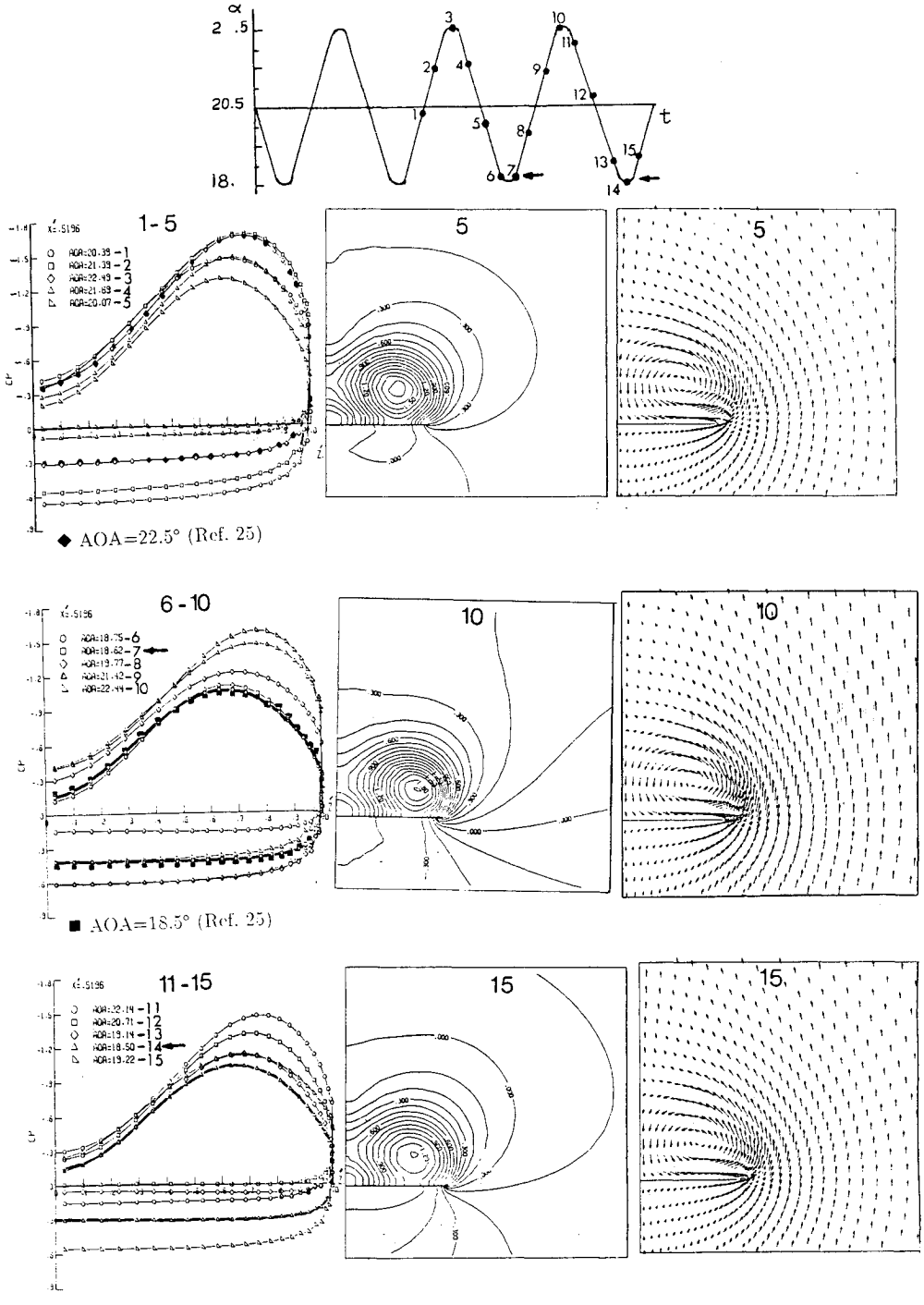

Fig. 5 Pitching motion, variation of surface pressure, static-pressure contours, and crossflow velocities for a sharp-edged delta wing undergoing pitching oscillation; $80\times38\times48$ cell, $M_\infty=0.3$, $\alpha_m=20.5$ deg, $\alpha_0=2$ deg, $k=3$, $AR=1$, $\epsilon_2=0.05$, $\epsilon_4=0.0025$, and $\epsilon_m=0.25$.

Concluding Remarks

The three-dimensional, unsteady, Euler equations in a moving frame of reference are solved by using an implicit approximately factored, finite-volume scheme. The computational applications cover steady, low-subsonic flow around a sharp-edged delta wing at a large angle of attack and unsteady, low-subsonic flow around the same wing undergoing a pitching oscillation about the same large angle of attack. The unsteady application presents pioneering results for the first time that we know. The steady-flow problem has been computed with two levels of numerical dissipation, and the results have been compared with each other and with the experimental data. The LD results give better agreement with the experimental data than those of HD results. However, fine-grid embedding is needed in the vortical regions. Moreover, the viscous terms must be added for accurate computations of the vortex-core regions (free-shear layers) and for the surface boundary-layer flow computations as well. Outside of these regions, Euler equations are adequate for computing the flowfield. This calls for urgent extension of the Euler/Navier-Stokes zonal scheme[16] to this problem. The results of the unsteady flow application show consistency, and they show periodic solution in the third cycle of oscillation. The present unsteady results have been compared with those of the flux-difference splitting scheme, and they are in good agreement. Although the code has also been verified previously with unsteady airfoil computation,[17] unsteady experimental data for vortex-dominated flows are urgently needed for benchmark comparison.

Acknowledgment

This research work is supported by NASA Langley Research Center under Grants NAG-1-846 and NAG-1-648. The authors would like to thank C. L. Rumsey for computing the pitching, delta-wing case using the CFL3D code.

References

[1]Whitlow, W., Jr., "Computational Unsteady Aerodynamics for Aeroelastic Analysis," NASA TM-100523, Dec. 1987.

[2]Ballhaus, W. F., and Goorjian, P. M., "Implicit Finite-Difference Computations of Unsteady Transonic Flows about Airfoils," *AIAA Journal*, Vol. 15, Dec. 1977, pp. 1728–1735.

[3]Edwards, J. W., Bland, S. R., and Seidel, D. A., "Experience with Transonic Unsteady Aerodynamic Calculations," NASA TM-86278, 1984.

[4]Batina, J. T., "Unsteady Transonic Algorithm Improvements for Realistic Aircraft Applications," AIAA Paper 88-0105, Jan. 1988.

[5]Chipman, R., and Jameson, A., "Full Conservative Numerical Solutions for Unsteady Irrotational Transonic Flow about Airfoils," AIAA Paper 79-1555, July 1979.

[6]Goorjian, P. M., "Implicit Computations of Unsteady Transonic Flow Governed by the Full Potential Equation in Conservation Form," AIAA Paper 80-0150, Jan. 1980.

[7]Ruo, S. Y., Malone, J. B., and Sankar, L. N., "Steady and Unsteady Full Potential Calculation for High and Low Aspect Ratio Supercritical Wings," AIAA Paper 86-0122, Jan. 1986.

[8]Batina, J. T., "Unsteady Transonic Small-Disturbance Theory Including Entropy and Vorticity Effects," AIAA Paper 88-2278-CP, April 1988.

[9]Whitlow, W., Jr., "Application of a Nonisentropic Full Potential Method to AGARD Standard Airfoils," AIAA Paper 88-0710, Jan. 1988.

[10]Howlett, J. T., and Bland, S. R., "Calculation of Viscous Effects on Transonic Flow for Oscillating Airfoils and Comparisons with Experiment," NASA TP-2731, Sept. 1987.

[11]Weinberg, B. C., and Shamroth, S. J., "Three-Dimensional Unsteady Viscous Flow Analysis Over Airfoil Sections," NASA CR-172368, 1984.

[12]Kandil, O. A., and Chuang, H. A., "Influence of Numerical Dissipation on Computational Euler Equations for Vortex-Dominated Flows," *AIAA Journal*, Vol. 25, Nov. 1987, pp. 1426–1434.

[13]Kandil, O. A., and Chuang, H. A., "Computation of Steady and Unsteady Vortex-Dominated Flows," *AIAA Journal*, Vol. 26, No. 5, May 1988, pp. 524–531.

[14]Kandil, O. A., and Chuang, H. A., "Unsteady Vortex-Dominated Flows Around Maneuvering Wings Over a Wide Range of Mach Numbers," AIAA Paper 88-0317, Jan. 1988.

[15]Holst, T. L., Gundy, K. L., Flores, J., Chanderjian, N. M., Kaynak, U., and Thomas, S. D., "Numerical Solution of Transonic Wing Flows Using an Euler/Navier-Stokes Zonal Approach," AIAA Paper 85-1640, July 1985.

[16]Liu, C. H., Wong, T. C., and Kandil, O. A., "Separation-Bubble Flow Solution Using Euler/Navier-Stokes Zonal Approach with Downstream Compatibility Conditions," *Journal of Scientific Computing*, Vol. 3, No. 2, 1988, pp. 121–137.

[17]Kandil, O. A., and Chuang, H. A., "Unsteady Transonic Airfoil Computation Using Implicit Euler Scheme on Body-Fixed Grid," *AIAA Journal*, Vol. 27, Aug. 1989, pp. 1031–1037.

[18]Anderson, W. K., Thomas, J. L., and Runsey, C. L., "Extension and Applications of Flux-Vector Splitting to Unsteady Calculations on Dynamic Meshes," AIAA Paper 87-1152-CP, 1987.

[19]Visbal, M. R., and Shang, J. S., "Numerical Investigation of the Flow Structure Around a Rapidly Pitching Airfoils," AIAA Paper 87-1424, June 1987.

[20]Rumsey, C. L., and Anderson, W. K., "Some Numerical and Physical Aspects of Unsteady Navier-Stokes Computations Over Airfoils Using Dynamic Meshes," AIAA Paper 88-0329, Jan. 1988.

[21]Landon, R., "NACA 0012 Oscillatory and Transient Pitching," *Compendium of Unsteady Aerodynamic Measurements*, AGARD-R-702, 1982.

[22]Hummel, O., "On the Vortex Formation Over a Slender Wing at Large Angles of Incidence," AGARD CP-247, Jan. 1979, pp. 15.1–15.17.

[23]Kandil, O. A., Chuang, H. A., and Shifflette, J. M., "Finite-Volume Euler and Navier-Stokes Solvers for Three-Dimensional and Conical Vortex Flows Over Delta Wings," AIAA Paper 87-0041, Jan. 1987.

[24]Kandil, O. A., and Chuang, H. A., "Prediction of Unsteady Loads on Manuevering Delta Wings Using Time-Accurate Euler Schemes," AIAA Paper 88-2280-CP, April 1988, pp. 504–512.

[25]Rumsey, C. L., private communication, July 1988.